

Vanadium (III) Oxide/Carbon Core/Shell Hybrids as an Anode for Lithium-Ion Batteries

Öznil Budak,^[a, b] Pattarachai Srimuk,^[a, b] Aura Tolosa,^[a, b] Simon Fleischmann,^[a, b] Juhan Lee,^[a, b] Stefan W. Hieke,^[c] Anna Frank,^[c] Christina Scheu,^[c, d] and Volker Presser^{*[a, b]}

We present a facile two-step synthesis of vanadium (III) oxide/carbon core/shell hybrid material for application as lithium-ion battery electrode. The first step is a thermal treatment of a mixture of vanadium carbide (VC) and $\text{NiCl}_2 \cdot 6\text{H}_2\text{O}$ at 700 °C in an inert gas atmosphere. Elemental nickel obtained from decomposing $\text{NiCl}_2 \cdot 6\text{H}_2\text{O}$ served as a catalyst to trigger the local formation of graphitic carbon. In a second step, residual nickel was removed by washing the material in aqueous HCl. By replacing $\text{NiCl}_2 \cdot 6\text{H}_2\text{O}$ with anhydrous NiCl_2 , we obtained a hybrid material of vanadium carbide-derived carbon and a

vanadium carbide core. Material characterization revealed a needle-like morphology of the rhombohedral V_2O_3 along with two carbon species with a different degree of graphitic ordering. We varied the $\text{NiCl}_2 \cdot 6\text{H}_2\text{O}$ -to-VC ratio, and the optimized material yielded a capacity of 110 $\text{mAh} \cdot \text{g}^{-1}$ at 2.5 $\text{A} \cdot \text{g}^{-1}$ which increased to 225 $\text{mAh} \cdot \text{g}^{-1}$ at 0.1 $\text{A} \cdot \text{g}^{-1}$ after 500 cycles in the potential range of 0.01–3.00 V vs. Li/Li⁺. This enhanced performance is in stark contrast to the loss of lithium uptake capacity when using commercially available V_2O_3 mixed with carbon black, where 93 % of the initial capacity was lost after 50 cycles.

1. Introduction

Lithium-ion batteries (LIBs) are attractive for electrochemical energy storage due to their high energy density and efficiency.^[1,2] The continuous research and development on LIBs not only consider the storage capacity and the ability to handle high charge/discharge rates, but also safety, cost, and cycle life.^[3–5] As a critical component of LIBs, the structural and electrochemical properties of the electrode materials strongly influence the overall device performance.^[2,6, 7] Graphite, silicon, titanium dioxide, and lithium titanate have been thoroughly investigated for LIBs anodes.^[8–11] With a specific capacity of 372 $\text{mAh} \cdot \text{g}^{-1}$, graphite anodes have been employed in commercial LIB devices.^[1] However, graphite anodes suffer from safety hazards because metallic lithium can be easily electroplated during charging, particularly at a high current rate and low temperatures.^[7,12] Silicon anodes have a much higher theoretical capacity of about 4200 $\text{mAh} \cdot \text{g}^{-1}$ but provide at present only poor capacity retention due to substantial

volumetric changes during cycling.^[13] Anodes composed of TiO_2 (rutile or anatase) and $\text{Li}_4\text{Ti}_5\text{O}_{12}$ exhibit higher rate capability and structure stability but their use remains restricted by their lower theoretical capacity of 168–175 $\text{mAh} \cdot \text{g}^{-1}$.^[9,14,15]

Capitalizing on different vanadium oxidation states, V_2O_5 , VO_2 , and V_2O_3 , have been explored as LIB cathodes and anodes.^[16–19] Among these, V_2O_5 is an attractive LIB cathode material due to the high theoretical capacity of 294 $\text{mAh} \cdot \text{g}^{-1}$ in the range of 4.0–2.0 V vs. Li/Li⁺.^[20,21] A slightly higher capacity of 323 $\text{mAh} \cdot \text{g}^{-1}$ has been reported for VO_2 in the range of 1.8–3.8 V vs. Li/Li⁺.^[22] V_2O_3 is a promising anode candidate for LIBs but there have been only very few studies exploring V_2O_3 as an anode material for LIBs so far.^[23–26] The current state of the art assumes that V_2O_3 undergoes structural volume change during galvanostatic charge/discharge cycling; this effect and the low electronic conductivity explain the poor cycling stability.^[25] For example, there is a 50–60 % capacity loss of bulk V_2O_3 after 50–100 charge/discharge cycles.^[23,25] Additionally, it remains unclear from the literature if it is intercalation or conversion by which mechanism V_2O_3 operates as an anode in LIBs. For example, Shi et al. (Ref.^[24]) assumed that V_2O_3 is a typical conversion type anode material for LIBs with a theoretical capacity of 1070 $\text{mAh} \cdot \text{g}^{-1}$. Another mechanism is intercalation reported by Sun et al. (Ref.^[25]) and McNulty et al. (Ref.^[27]) as the theoretical capacity of 356 $\text{mAh} \cdot \text{g}^{-1}$ and 179 $\text{mAh} \cdot \text{g}^{-1}$ for $\text{Li}_1\text{V}_2\text{O}_3$, respectively.

To overcome the limited performance of bulk V_2O_3 mixed with a conductive additive, recent studies have explored hybrid electrodes.^[18] In composite electrodes, mechanically admixed carbon serves as an electrically conducting agent between the metal oxide and the current collector. Alternatively, the hybrid electrode architecture employs a nanoscopic chemical blending of the metal oxide phase with carbon, and the resulting materials provide improved electrochemical performance.^[18,28,29]

[a] Ö. Budak, P. Srimuk, A. Tolosa, S. Fleischmann, Dr. J. Lee, Prof. Dr. V. Presser
INM – Leibniz Institute for New Materials
Campus D2 2, 66123 Saarbrücken, Germany
E-mail: volker.presser@leibniz-inm.de

[b] Ö. Budak, P. Srimuk, A. Tolosa, S. Fleischmann, Dr. J. Lee, Prof. Dr. V. Presser
Department of Materials Science and Engineering
Saarland University
Campus D2 2, 66123 Saarbrücken, Germany

[c] Dr. S. W. Hieke, Dr. A. Frank, Prof. Dr. C. Scheu
Max-Planck-Institut für Eisenforschung GmbH
Nanointerfaces
Max-Planck-Straße 1, 40237 Düsseldorf, Germany

[d] Prof. Dr. C. Scheu
Materials Analytics
RWTH Aachen University
Kopernikusstraße 10, 52074 Aachen, Germany

 Supporting information for this article is available on the WWW under
<https://doi.org/10.1002/batt.201800115>

Studies on V_2O_3 /carbon hybrids have reported a range of capacity values, and while some works used the material as a cathode, others used it as a LIB anode. For example, Odani et al. investigated carbon-coated V_2O_3 as a LIB cathode with a low capacity of $25 \text{ mAh}\cdot\text{g}^{-1}$ in the voltage range of $2.0\text{--}4.0 \text{ V}$ vs. Li/Li^+ .^[30] As found by Sun et al.,^[25] ordered lamellar V_2O_3 provides a capacity of about $120 \text{ mAh}\cdot\text{g}^{-1}$ with the cutoff voltage of 0.3 V and 1.5 V vs. Li/Li^+ , and Jiang et al. (Ref.^[23]) reported carbon-coated yolk-shell V_2O_3 microspheres as an anode material with the capacity of $437 \text{ mAh}\cdot\text{g}^{-1}$ at the specific current of $0.1 \text{ mA}\cdot\text{g}^{-1}$ in the voltage window of $0.1\text{--}3.0 \text{ V}$ vs. Li/Li^+ . The porous $\text{V}_2\text{O}_3/\text{C}$ composite material was reported with a discharge capacity of $283 \text{ mAh}\cdot\text{g}^{-1}$ in the voltage range of $0\text{--}3 \text{ V}$ vs. Li/Li^+ by Shi et al. (Ref.^[24]). The reversible capacity of $536 \text{ mAh}\cdot\text{g}^{-1}$ from composite V_2O_3 -ordered mesoporous carbon at a current density of $1 \text{ A}\cdot\text{g}^{-1}$ in the voltage range of $0.02\text{--}3 \text{ V}$ was achieved by Zeng et al. (Ref.^[31]).

Considering the promising performance of hybrid materials, we have previously developed the top-down synthesis of V_2O_5 /carbide-derived carbon core/shell particles.^[20] In our earlier work, we used a three-step synthesis: first, a mixture of vanadium carbide and $\text{NiCl}_2\cdot6\text{H}_2\text{O}$ was heated in a vacuum, and the evolving chlorine gas extracted vanadium from the outer regions of the carbide grains; this leads to the formation of a carbide-derived carbon shell. The latter is sufficiently nanoporous so that ion transport across the carbon shell is accomplished. Second, residual nickel from the thermal decomposition of $\text{NiCl}_2\cdot6\text{H}_2\text{O}$ was removed by washing in aqueous HCl. Third, the residual carbide core was transformed to V_2O_5 by thermal oxidation at $450\text{--}600^\circ\text{C}$ while the carbide-derived carbon shell was maintained. In our present work, we significantly simplify the synthesis by using only one thermal treatment step that, concurrently, yields a carbide-derived carbon shell and a vanadium oxide core. The produced material is freed from residual nickel by simple washing with aqueous HCl and can be used as a LIB anode with promising cycling performance.

Experimental

Material Synthesis

$\text{V}_2\text{O}_3/\text{VC-CDC}$ and VC/VC-CDC core/shell materials were synthesized by using a solid mixture of VC powder (purity 99.9%, $<2 \mu\text{m}$, Sigma Aldrich) and two different precursors, $\text{NiCl}_2\cdot6\text{H}_2\text{O}$ (purity 99.5%, Alfa Aesar) and NiCl_2 (purity 99.99%, Sigma Aldrich), respectively.

The stoichiometric amounts of 2.0 mol, 2.5 mol, and 3.0 mol of $\text{NiCl}_2\cdot6\text{H}_2\text{O}$ per 1 mol of VC were mixed and ground in a mortar. The mixtures were transferred into quartz glass crucible and placed in a quartz tube furnace (HTRH, Gero) which was continuously flushed with Ar gas with a flow rate of $50 \text{ cm}^3\cdot\text{min}^{-1}$. The furnace was heated from room temperature to 700°C with a heating rate of $2.5^\circ\text{C}\cdot\text{min}^{-1}$ and held at the annealing temperature for 3 h. Afterward, the samples were cooled to room temperature. The outlet of the tube was fed through a reservoir filled with aqueous 5 M NaOH to neutralize the gaseous reaction products (esp. CO_2 and HCl, see Supporting Information, Figure S1). The resulting

material was washed with 200 mL of aqueous 3 M HCl to remove the residual elemental nickel. The solution was stirred overnight and washed with an excess amount of distilled water until the pH of the discarded water was neutral. The filtered product was dried at 80°C overnight. The final products of the $\text{V}_2\text{O}_3/\text{VC-CDC}$ syntheses are labeled $\text{V}_2\text{O}_3/\text{VC-CDC-1:2}$, $\text{V}_2\text{O}_3/\text{VC-CDC-1:2.5}$, and $\text{V}_2\text{O}_3/\text{VC-CDC-1:3}$.

For the synthesis of the VC/VC-CDC core/shell material, we modified the procedure used for the synthesis of $\text{V}_2\text{O}_3/\text{VC-CDC}$ core/shell material by using a stoichiometric ratio of NiCl_2 and VC of 2:1 and a synthesis temperature of 1000°C .

Structural Characterization

X-ray powder diffraction (XRD) patterns were recorded using a D8 Discover diffractometer (Bruker AXS) with $\text{Cu-K}\alpha$ radiation ($\lambda = 1.5406 \text{ \AA}$) and a Goebel mirror in point focus (0.5 mm). The system was calibrated with LaB_6 (purity 99%, Sigma Aldrich), and the samples were placed on a single sapphire crystal. A VANTEC-500 (Bruker AXS) 2D detector was positioned at 20° , 40° , 60° , 80° , and 100° 2θ with a measurement time of 7 min per step. Rietveld refinement analyses were performed by using the software TOPAS from Bruker.

Raman spectra were recorded with a Renishaw inVia Raman Microscope equipped with an Nd-YAG laser with an excitation wavelength of 532 nm and a power of 0.05 mW at the surface of the sample, using an objective lens with a numeric aperture of 0.75. The spectra of the samples were recorded with 20 accumulations and 30 s acquisition time. All spectra were normalized to 100%, and fitting was achieved assuming Voigt peak profiles for the D-mode, G-mode, and amorphous carbon.

Gas sorption analysis (GSA) was conducted to obtain a specific surface area (SSA), and pore volume of the samples. We carried out the measurements with an Autosorb-6B system (Quantachrome) using nitrogen gas at -196°C in a relative pressure range from 0.008 to 1.0 in 76 steps. Prior to the measurements, the powder samples were degassed at 250°C and 10^2 Pa for 12 h. The SSA was calculated using the Brunauer-Emmett-Teller (BET) equation^[32] in the linear pressure range (ca. 0.01–0.1) with the ASiQwin-software. The values for the total pore volume were obtained at a relative pressure of $P/P_0 = 0.95$. Since the materials were hybrids of either VC-CDC and VC or VC-CDC and V_2O_3 , the direct use of density functional theory kernels designed for pure carbon samples prohibited the further porosity analysis regarding the pore size distribution.^[33] Instead, we limited the porosity analysis to the quantification of the BET surface area and the total pore volume.

The sample morphology was characterized by scanning electron microscopy (SEM) using a JEOL JSM 7500F at an acceleration voltage of 3 kV. The samples were fixed on a steel sample holder by using sticky carbon tape. The chemical compositions of the samples were quantified by energy dispersive X-ray (EDX) spectroscopy with an X-Max-150 detector (Oxford Instruments) attached to the SEM chamber. The spectra of fifty spots were measured with an acceleration voltage of 14 kV and averaged.

Transmission electron microscopy (TEM) investigations were carried out by using a JEOL JEM-2100F instrument operated at 200 kV. Scanning TEM (STEM) was performed on a probe-corrected FEI Titan Themis 60-300 X-FEG S/TEM instrument operated at 300 kV equipped with an FEI Super-X windowless EDX system with 4 synchronized silicon drift detectors from Bruker. The samples were dispersed in isopropanol or ethanol through sonication for 2 min and drop-casted onto a copper grid with a lacey carbon film.

Thermogravimetric analysis coupled with mass spectrometry (TGA-MS) was carried out up to 1000 °C with a heating rate of 2.5 °C·min⁻¹ in argon with a STA449F3 Jupiter and QMS 403 C Aëlos from Netzsch for a mixture of 1 mol VC per 2 mol of NiCl₂·6H₂O.

Electrochemical Characterization

To prepare electrodes, 90 mass% of the active material was blended in a mortar with 10 mass% polyvinylidene fluoride (PVdF, Alfa Aesar) as a binder. N-methyl-2-pyrrolidone (NMP, Sigma Aldrich) was added to the solid mixture until the slurry reached a sufficient viscosity; the slurry was then coated on a Cu foil at a wet thickness of 150 µm. The coated slurry was dried in a vacuum oven at 110 °C overnight. The packing density of the electrode was adjusted by dry-pressing in the rolling machine (HR01 hot rolling machine, MTI) and cut to circular shape with a diameter of 12 mm. The average mass loading was 2.6 mg·cm⁻² with a dry thickness of 96 µm.

For comparison, we also made electrodes using commercially available V₂O₃ (Sigma Aldrich) which consisted of 80 mass% V₂O₃, 10 mass% carbon black (C65 from Imerys Graphite & Carbon), and 10 mass% PVdF following the same preparation procedure as for the other materials. These electrodes are labeled "com-V₂O₃" to reflect the commercial source of V₂O₃ and the composite nature of these electrodes (i.e., a physical mixture of the metal oxide and the conductive additive).

For electrochemical measurements, 2032-type coin cells were assembled in an argon-filled glove box (O₂, H₂O < 1 ppm). We used lithium foil (diameter of 12 mm) as a reference and counter electrode, 1 M lithium hexafluorophosphate (LiPF₆) in an ethylene carbonate (EC) and dimethyl carbonate (DMC) mixture in the ratio EC:DMC (1:1 by volume) as electrolyte (LP 30, BASF), and two layers of Celgard 2325 as separator with a diameter of 18 mm.

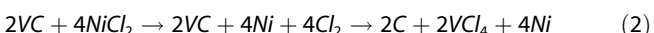
Cyclic voltammetry (CV) was carried out using a VMP300 system from Bio-Logic multichannel potentiostat in the potential range of 0.01–3.00 V vs. Li/Li⁺ at a scan rate of 0.05 mV·s⁻¹. An Arbin system was used for galvanostatic charge/discharge cycling with potential limitation (GCPL) in the range of 0.01–3.00 V vs. Li/Li⁺ at room temperature. The calculated specific capacity of the samples is based on the active mass of the electrode material including carbon mass of the hybrid materials. For the com-V₂O₃ electrode, the specific capacity was normalized by just the metal oxide mass. The capacity retention test was performed during galvanostatic charge/discharge cycling at 0.1 A·g⁻¹ from 0.01 V to 3.00 V vs. Li/Li⁺ in half-cell configuration.

To better understand the structural changes of the material during electrochemical benchmarking, post mortem XRD and Raman spectroscopy analyses were carried out for the electrodes by disassembling the cells after cycling stability testing. To understand the intermediate structural changes, the cells were charged/discharged at the specific current at 0.1 A·g⁻¹ for 40 cycles. Thereafter, the cycled cells were held at 1.5 V, 0.75 V, and 0.01 V vs. Li/Li⁺ for the lithiation and at 0.75 V, 1.5 V, and 3.0 V for the delithiation. Those six cells were disassembled and gently cleaned by using propylene carbonate (PC). The washed electrodes were subjected to XRD measurements.

2. Results and Discussion

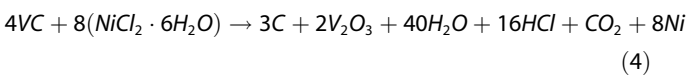
2.1. Material Synthesis Concept

Thermal annealing of nickel chloride leads to its decomposition and the evolution of chlorine gas.^[20] In the presence of a metal carbide like vanadium carbide, the evolving chlorine selectively reacts with the metal ions, producing gaseous vanadium chloride. This process leaves behind nanoporous carbide-derived carbon (CDC) as the solid reaction product.^[20,34, 35] For example, the mixture of vanadium carbide and NiCl₂·6H₂O leads to the formation of VC-CDC when the annealing is carried out in a vacuum furnace.^[20] As seen from Equation (1–3), this reaction considers the decomposition of NiCl₂ which is obtained via the dehydration of NiCl₂·6H₂O during the thermal treatment (700 °C). Nickel is a by-product of the process and can be removed from the material by aqueous HCl washing because the resulting NiCl₂ phase is water soluble. Adjusting the molar ratio of chlorine to carbide, a VC core can be maintained while a shell of nanoporous CDC is being produced. In a subsequent step, the vanadium carbide core is then transformed to vanadium oxide, while maintaining largely the CDC shell. The combination of a metal oxide core for lithium-ion intercalation and an electrically conductive outer carbon shell make this core/shell hybrid material attractive for electrochemical energy storage.^[18]



The need for two separate thermal treatment steps, one for the CDC-process and a subsequent one for the carbide oxidation, complicates the fabrication of this core/shell hybrid material. This applies in particular because the two thermal treatment steps are separated by washing the carbide/carbon core/shell material in aqueous HCl.

The present work uses the same precursor as our previous work (i.e., VC and NiCl₂·6H₂O) but carries out the annealing process in an inert gas atmosphere (argon) instead of a low vacuum. By this way, we avoid the rapid removal of desorbing water and enable a reaction per Equation (4).



In addition, we also carried out experiments with anhydrous nickel chloride (NiCl₂), which should only result in CDC formation via Equation (2).

To understand the mechanism of V₂O₃ formation, we carried out a thermogravimetric analysis with a coupled mass spectrometer (Figure S1). The mass loss below 100 °C aligns with the desorption of surface water, as indicated by the increase of the H₂O signal. As the temperature was increased to 200 °C, a significant amount of water was produced by the

release of crystal water from NiCl_2 . Additionally, gaseous HCl was detected at 100–200°C suggesting the loss of chloride, which possibly reacts with the as-produced water to form hydroxyl radicals. The absence of OH^- in our measurements indicates that resulting hydroxyl radicals react on the surface of vanadium carbide yielding O_2 gas as the final product. Apparently, the loss of chloride and crystal water continued as the temperature was further increased. Oxygen leads to the formation of vanadium (III) oxide at around 700°C, which aligns with a decrease of the O_2 signal at this temperature.

2.2. Material Characterization

We first analyzed the VC/VC-CDC sample synthesized from the mixture of anhydrous NiCl_2 and vanadium carbide by XRD. The synthesis mechanism of VC/VC-CDC follows Equation (2), and we obtained residual cubic vanadium carbide (PDF 01-089-2608, Figure 1A and Table S1) with a unit cell of $a=8.34\text{ \AA}$ with characteristic Bragg reflections at 37.4° , 63.0° , and 43.4° 2θ . In addition, the Bragg reflection at 26.2° indicates carbon (hexagonal graphite: PDF 01-089-7213) and the presence of vanadium carbide-derived carbon (VC-CDC) was also confirmed by Raman spectroscopy (Figure 1B and Table 1).^[34] The Raman

Table 1. Raman spectra analysis of the D and G-modes. FWHM = full-width at half-maximum.

| Sample | Mode | Position [cm ⁻¹] | FWHM [cm ⁻¹] | I_D/I_G |
|---|--------|------------------------------|--------------------------|-----------|
| com-V ₂ O ₃ | D-mode | 1354 | 109 | 2.02 |
| | G-mode | 1606 | 77 | |
| VC/VC-CDC | D-mode | 1349 | 61 | 0.9 |
| | G-mode | 1587 | 50 | |
| V ₂ O ₃ /VC-CDC-1:2 | D-mode | 1351 | 63 | 1.1 |
| | G-mode | 1593 | 66 | |
| V ₂ O ₃ /VC-CDC-1:2.5 | D-mode | 1349 | 73 | 1.1 |
| | G-mode | 1591 | 61 | |
| V ₂ O ₃ /VC-CDC-1:3 | D-mode | 1348 | 109 | 2.1 |
| | G-mode | 1603 | 68 | |

spectra present two distinct peaks between 1200–2000 cm⁻¹, namely the D-mode and G-mode characteristic of incompletely graphitic carbon.^[36] The G-mode corresponds to the stretching vibration of pairs of sp² atoms in rings and chains, and the D-mode corresponds to the breathing mode of sp²-hybridized carbon rings, which is active in the presence of defects.^[37] Peak fitting of the Raman spectra (Table 1 and Figure S2A) yielded the D-mode position at 1349 cm⁻¹ and the G-mode position at 1587 cm⁻¹. In addition to that, carbon of the VC/VC-CDC sample presents a low I_D/I_G ratio of 0.9 and a full-width at half-

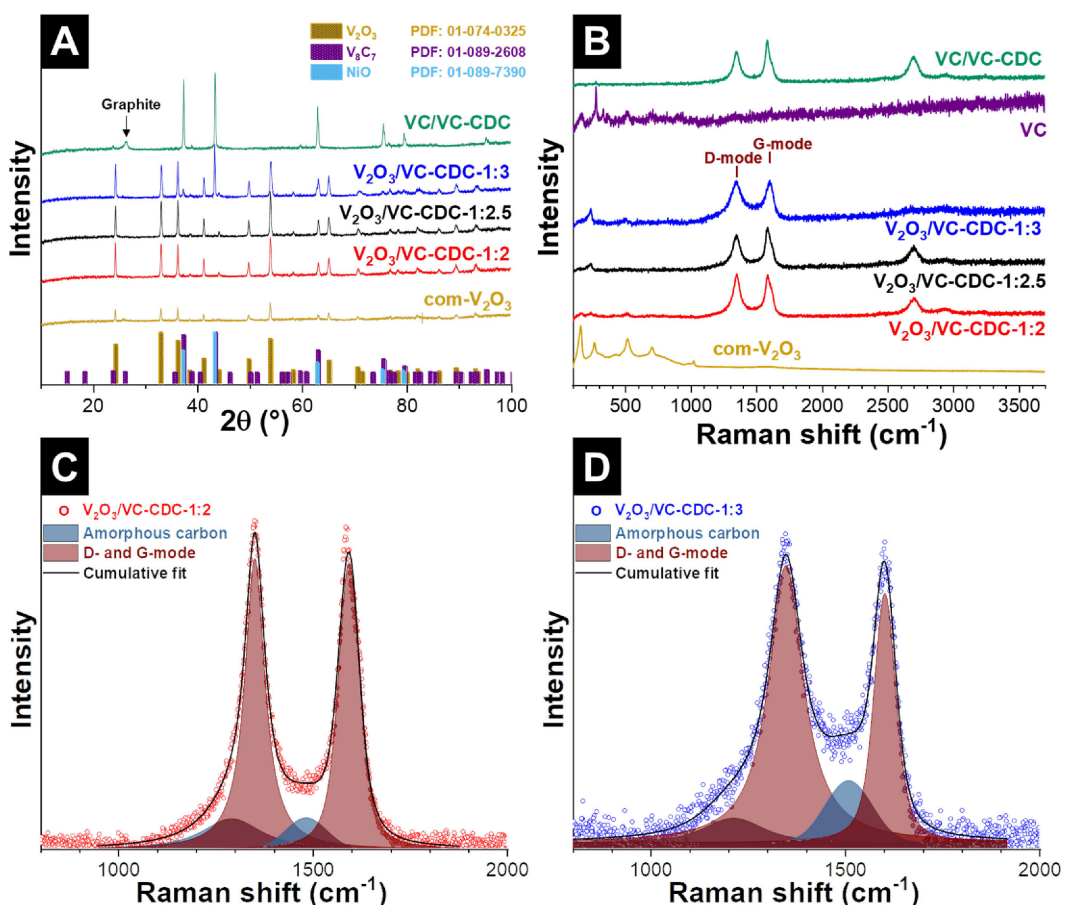


Figure 1. A) X-ray diffraction (XRD) pattern of the samples and the matched reflection position phases from the literature. B) Raman overview spectra of the samples. Fitted Raman spectra of V₂O₃/VC-CDC-1:2 (C) and V₂O₃/VC-CDC-1:3 (D).

maximum (FWHM) for the D- and G-mode with 61 cm^{-1} and 50 cm^{-1} , respectively.

In contrast to the use of anhydrous NiCl_2 , there is a different reaction outcome when mixing vanadium carbide with $\text{NiCl}_2 \cdot 6\text{H}_2\text{O}$. We used stoichiometric ratios of 1:2, 1:2.5, and 1:3 of VC to $\text{NiCl}_2 \cdot 6\text{H}_2\text{O}$ to investigate the influence of the amount of Ni on the degree of the graphitization of the carbon phase. As seen from the X-ray diffraction pattern (Figure 1A), we obtained vanadium oxide instead of VC-CDC. The sharp X-ray reflections at 24.3° , 33.1° , 41.2° , 43.3° , and 54.1° 2θ relate to karelianite-type rhombohedral V_2O_3 (PDF 01-074-0325). The higher energy barrier of the oxidation of nickel, compared to vanadium, prevented the formation of nickel oxide^[38] and no reflections related to NiO (PDF 01-089-7390) were identified by XRD (Figure 1A and Table S1). The only exception was $\text{V}_2\text{O}_3/\text{VC-CDC-1:3}$ where 21 mass % of NiO was found in the sample (as determined by Rietveld analysis).

Beside vanadium oxide, we also obtained carbon (VC-CDC) when using $\text{NiCl}_2 \cdot 6\text{H}_2\text{O}$. The Raman spectra of all $\text{V}_2\text{O}_3/\text{VC-CDC}$ samples (Figure 1B) show the characteristic broad peaks of incompletely graphitic carbon at around 1350 cm^{-1} (D-mode) and 1597 cm^{-1} (G-mode). Table 1 lists the positions of D- and G-mode, the full-width at half-maximum (FWHM), and the integral I_D/I_G intensity ratio of these peaks. Figure 1C–D presents the peak fitting of the Raman spectrum of $\text{V}_2\text{O}_3/\text{VC-CDC-1:2}$ and $\text{V}_2\text{O}_3/\text{VC-CDC-1:3}$. The $\text{V}_2\text{O}_3/\text{VC-CDC-1:3}$ sample has the highest I_D/I_G ratio of 2.1 and the widest FWHM for the D- and G-mode with 109 cm^{-1} and 68 cm^{-1} , respectively. In the case of $\text{V}_2\text{O}_3/\text{VC-CDC}$ samples, the higher degree of carbon disorder than that of

VC/VC-CDC aligns with the partial oxidation of carbon by oxygen during the in-situ synthesis (Figure S1B). Yet, the spatial resolution of Raman measurements of about $1\text{ }\mu\text{m}$ only provides us with an average quantitative assessment of all carbon present within the sampling volume. Therefore, we used transmission electron microscopy to better characterize carbon on a nanoscale.

When anhydrous nickel chloride thermally decomposed, we see that vanadium carbide particles (Figure 2A) were transformed to carbide cores engulfed by two carbon species: one with a lower degree of ordering (as typical for CDC obtained at 1000°C)^[39] and layered ribbons of graphitic carbon (Figure 2B–C). The overall structural ordering of VC-CDC is low, but graphitic layers and ribbons are seen throughout the VC/VC-CDC sample. The latter possibly impeded the diffusion of in-situ produced chlorine gas and kinetically slowed the carbide-to-carbon transformation.^[40] In our case, this is beneficial since we wanted to maintain a carbide core for the carbide-to-oxide formation. We explain the formation of two carbon phases with a very different degree of ordering by the catalytic properties of elemental nickel which is produced as a by-product of decomposing nickel chloride.^[41,42] Transmission electron micrographs confirm the presence of both carbon phases for all $\text{V}_2\text{O}_3/\text{VC-CDC}$ samples (Figure 2D–I). For these oxide/carbon hybrid materials, we find needle-like V_2O_3 surrounded by carbon, as evidenced by elemental mapping performed in STEM mode (Figure S4). Among the $\text{V}_2\text{O}_3/\text{VC-CDC}$ samples, a higher stoichiometric ratio of VC to $\text{NiCl}_2 \cdot 6\text{H}_2\text{O}$ yielded fewer needle-like V_2O_3 (Figure 2D–I).

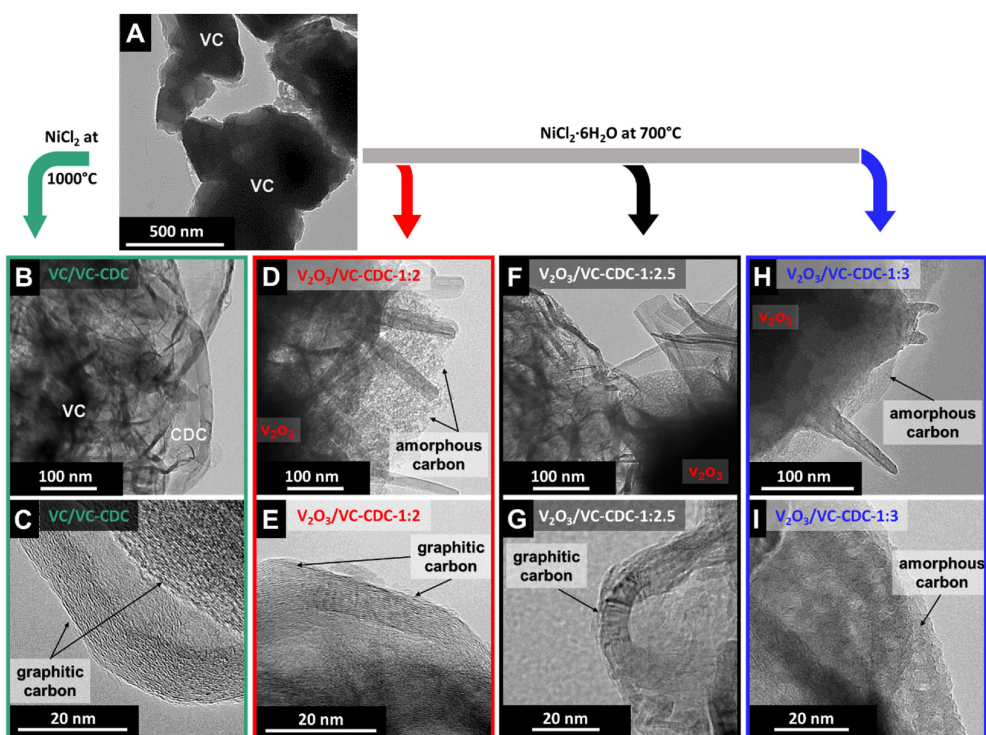


Figure 2. Bright field transmission electron micrographs of the initial vanadium carbide(A), of VC/VC-CDC (B–C), of $\text{V}_2\text{O}_3/\text{VC-CDC-1:2}$ (D–E), of $\text{V}_2\text{O}_3/\text{VC-CDC-1:2.5}$ (F–G), and of $\text{V}_2\text{O}_3/\text{VC-CDC-1:3}$ (H–I).

Elemental analysis of the samples on a more global scale was performed by EDX measurements in the SEM (Table 3). The highest carbon content (ca. 33 mass %) was found for VC/VC-CDC, and the amount of carbon decreased for $\text{V}_2\text{O}_3/\text{VC}-\text{CDC}$ with the increasing amount of $\text{NiCl}_2 \cdot 6\text{H}_2\text{O}$. The lowest value of carbon was found for $\text{V}_2\text{O}_3/\text{VC}-\text{CDC}-1:3$ with ca. 8 mass %. The decreased carbon content aligns with an increased amount of oxidizing species being mobilized during the decomposition of $\text{NiCl}_2 \cdot 6\text{H}_2\text{O}$.

We carried out nitrogen gas sorption to characterize the porosity of the synthesized materials, and the data are presented in Table 2. As seen from the sorption isotherm

| Table 2. Porosity data obtained from nitrogen gas sorption analysis at -196°C . | | |
|---|---|--|
| Sample | SSA_{BET} [$\text{m}^2 \cdot \text{g}^{-1}$] | Total pore volume [$\text{cm}^3 \cdot \text{g}^{-1}$] |
| VC/VC-CDC | 125 | 0.21 |
| $\text{V}_2\text{O}_3/\text{VC}-\text{CDC}-1:2$ | 71 | 0.08 |
| $\text{V}_2\text{O}_3/\text{VC}-\text{CDC}-1:2.5$ | 24 | 0.03 |
| $\text{V}_2\text{O}_3/\text{VC}-\text{CDC}-1:3$ | 16 | 0.02 |

Table 3. Elemental analysis of the samples by EDX.

| Sample | Carbon [mass %] | Oxygen [mass %] | Vanadium [mass %] | Nickel [mass %] |
|---|--------------------|--------------------|----------------------|--------------------|
| VC/VC-CDC | 32.5 ± 14.2 | 11.8 ± 6.7 | 53.7 ± 14.8 | 0.5 ± 0.4 |
| $\text{V}_2\text{O}_3/\text{VC}-\text{CDC}-1:2$ | 15.8 ± 6.2 | 30.7 ± 7.3 | 52.1 ± 10.2 | 0.9 ± 1.0 |
| $\text{V}_2\text{O}_3/\text{VC}-\text{CDC}-1:2.5$ | 13.3 ± 7.0 | 21.6 ± 6.9 | 63.2 ± 9.4 | 2 ± 1.1 |
| $\text{V}_2\text{O}_3/\text{VC}-\text{CDC}-1:3$ | 7.6 ± 4.3 | 22.3 ± 8.1 | 60.6 ± 16.2 | 9.4 ± 5.0 |

(Figure S5), all samples showed a type II isotherm which is indicative of macroporous materials with some mesopores.^[43] VC/VC-CDC had a total pore volume of $0.21 \text{ cm}^3 \cdot \text{g}^{-1}$ with an SSA_{BET} of $125 \text{ m}^2 \cdot \text{g}^{-1}$. Among the metal oxide/carbon hybrids, the $\text{V}_2\text{O}_3/\text{VC}-\text{CDC}-1:2$ sample had the largest SSA_{BET} of $71 \text{ m}^2 \cdot \text{g}^{-1}$ and the smallest surface area was found for $\text{V}_2\text{O}_3/\text{VC}-\text{CDC}-1:3$ ($16 \text{ m}^2 \cdot \text{g}^{-1}$). This trend aligns with the amount of

carbon and shows that the porosity is mostly accomplished by nanoporous carbon, whereas a small specific surface area is associated with the metal oxide domains.

2.3. Electrochemical Analysis

For the electrochemical characterization, we used electrodes made from the as-synthesized VC/VC-CDC and $\text{V}_2\text{O}_3/\text{VC}-\text{CDC}$ materials and added 10 mass% of PVdF binder but no conductive additive. The latter was possible because the presence of VC-CDC by itself was sufficient to provide a conductive pathway for electron transport in the samples. For comparison, we also cast electrodes of a mixture of 80 mass% commercial V_2O_3 , 10 mass% of carbon black, and 10 mass% of PVdF; these electrodes are labeled com- V_2O_3 . Using 1 M LiPF₆ in an EC/DMC as the electrolyte, we tested all materials in a half-cell configuration with an oversized lithium counter electrode.

The initial cycle performance was analyzed by cyclic voltammetry (CV) in the range of 0.01–3.00 V vs. Li/Li⁺ at a scan rate of $0.05 \text{ mV} \cdot \text{s}^{-1}$ to characterize the reduction and oxidation potentials of the samples (Figure 3). The largest amount of charge was passed for $\text{V}_2\text{O}_3/\text{VC}-\text{CDC}-1:2$, and the cyclic voltammograms of all samples exhibit broad cathodic and anodic peaks. Near 0.01 V vs. Li/Li⁺, the increased current of all samples results from intercalation and deintercalation of lithium-ions into graphitic carbon.^[44] The other possible current peaks relate to the multistep reduction of V³⁺ to lower valence states.^[23] The cathodic peak at 0.70 V may be associated with the formation of Li₂O, and the complex solid electrolyte interface (SEI);^[45] its disappearance after the first cycle aligns with the formation of a stable SEI (Figure 3B). In addition, the $\text{V}_2\text{O}_3/\text{VC}-\text{CDC}-1:3$ sample shows a cathodic peak at 0.40 V (Figure 3A), and it is possible that the presence of NiO leads to a shift in the potential for SEI formation.

With contributions from the lithiation/delithiation of the V_2O_3 domains and a small contribution from carbon lithiation/

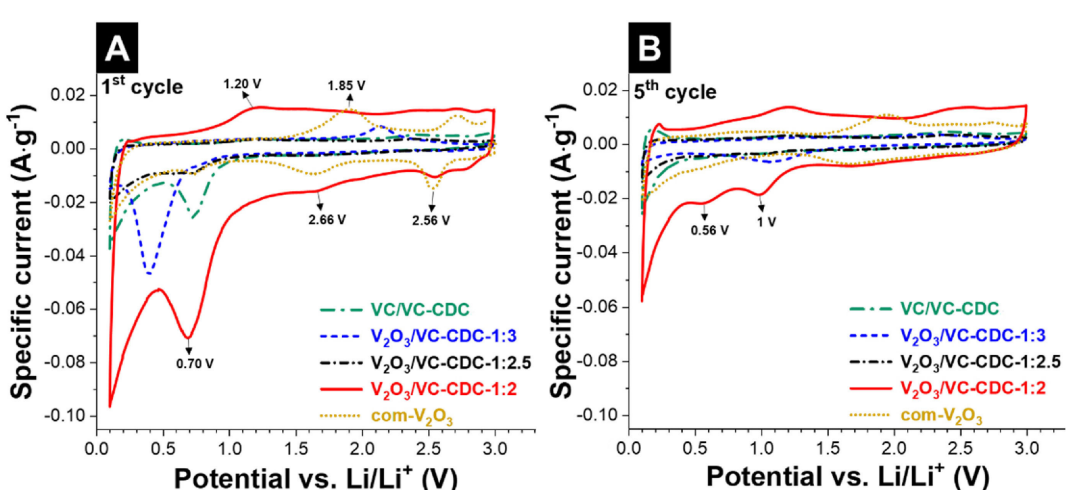


Figure 3. Cyclic voltammograms of the samples from the 1st cycle (A) and the 5th cycle (B) in the range of 0.01–3.00 V vs. Li/Li⁺ at a scan rate of $0.05 \text{ mV} \cdot \text{s}^{-1}$.

delithiation (Table 3), we can express the Li intercalation/deintercalation process by Equations (5) and (6):^[25]



We further characterized the electrochemical performance with galvanostatic charge/discharge cycling at a specific current of $0.1 \text{ A} \cdot \text{g}^{-1}$ in the voltage range from 0.01 V to 3.00 V vs. Li/Li⁺. The voltage profiles of the 10th cycle are found in Figure 4A. The results agree with the electrochemical behavior seen with cyclic voltammetry: the highest charge storage capacity is seen for V₂O₃/VC-CDC-1:2 (157 mAh·g⁻¹), followed by VC-CDC (76 mAh·g⁻¹), com-V₂O₃ (44 mAh·g⁻¹), V₂O₃/VC-CDC-1:2.5 (39 mAh·g⁻¹), and V₂O₃/VC-CDC-1:3 (20 mAh·g⁻¹). In general, we see the combination of (multistep) lithiation of V₂O₃. Below 0.1 V vs. Li/Li⁺, there is an additional charge contribution related to lithiation of carbon.

The rate handling performance of all samples was characterized by galvanostatic charge/discharge cycling at specific currents in the range of $0.01\text{--}10 \text{ A} \cdot \text{g}^{-1}$ in the voltage window of 0.01–3.00 vs. Li/Li⁺ (Figure 4B). After the first cycle at the specific current of $0.01 \text{ A} \cdot \text{g}^{-1}$, V₂O₃/VC-CDC-1:2 demonstrates the highest capacity of about 187 mAh·g⁻¹, which is higher than the capacity of the com-V₂O₃ composite electrode (126 mAh·g⁻¹), and V₂O₃/VC-CDC-1:2.5 preserves the lowest reversible capacity of 51 mAh·g⁻¹. The initial capacity of V₂O₃/VC-CDC-1:3 sample drops from 234 mAh·g⁻¹ to 66 mAh·g⁻¹ at the 5th cycle, which can be explained by the presence of bunsenite-type cubic NiO (Figure 1A): NiO is known to cause poor capacity retention for lithium-ion batteries due to its low electrical conductivity and substantial volume change during the conversion reaction.^[46] Accordingly, we confirm a rapid and complete loss of the reversible capacity of V₂O₃/VC-CDC-1:3 at higher rates.

As the specific current is increased, V₂O₃/VC-CDC-1:2 shows a good rate handling by maintaining values of about

110 mAh·g⁻¹ at $2.5 \text{ A} \cdot \text{g}^{-1}$ and about 40 mAh·g⁻¹ at $10 \text{ A} \cdot \text{g}^{-1}$ (Figure 4B). This performance is significantly better than com-V₂O₃ electrodes where only 18 mAh·g⁻¹ was maintained at $2.5 \text{ A} \cdot \text{g}^{-1}$; the latter corresponds with a capacity loss of 71% compared to the low-rate capacity. Electrodes of VC/VC-CDC showed a low initial capacity at $0.01 \text{ A} \cdot \text{g}^{-1}$ of 224 mAh·g⁻¹ during the first cycle and 117 mAh·g⁻¹ during the second cycle. Yet, this material maintained about 52% (40 mAh·g⁻¹) of the capacity at $0.5 \text{ A} \cdot \text{g}^{-1}$. In the absence of V₂O₃ domains, the charge storage capacity of VC/VC-CDC is limited to ion electro-sorption of lithium on the surface area, and below 0.1 V vs. Li/Li⁺ to lithium intercalation within graphitic domains of the carbon phase. With the presence of significant amounts of residual vanadium carbide acting as dead mass, the overall charge storage capacity is limited, but the short diffusion pathways for lithium to intercalate in the graphitic domains explain the high rate handling ability. The first-cycle performance of about 112 mAh·g⁻¹ of VC/VC-CDC is also fully restored after returning to the low rate of $0.01 \text{ A} \cdot \text{g}^{-1}$ after 45 cycles.

The cycling stability was tested in the voltage range of 0.01–3.00 V vs. Li/Li⁺ at a specific current of $0.1 \text{ A} \cdot \text{g}^{-1}$ (Figure 5). For

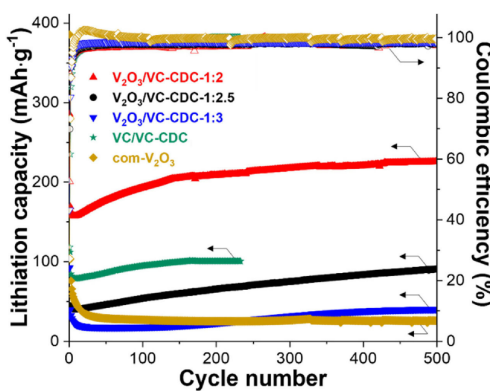


Figure 5. Cycling stability of the samples at $0.1 \text{ A} \cdot \text{g}^{-1}$.

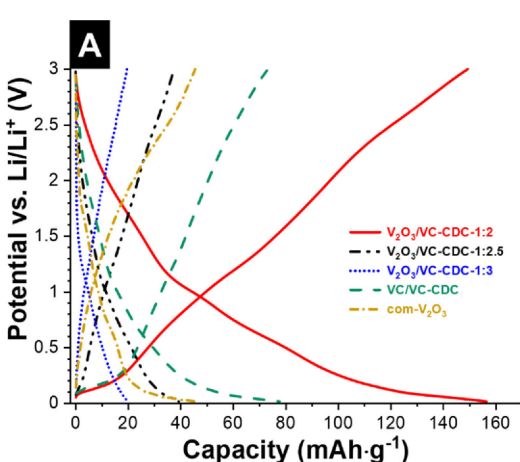
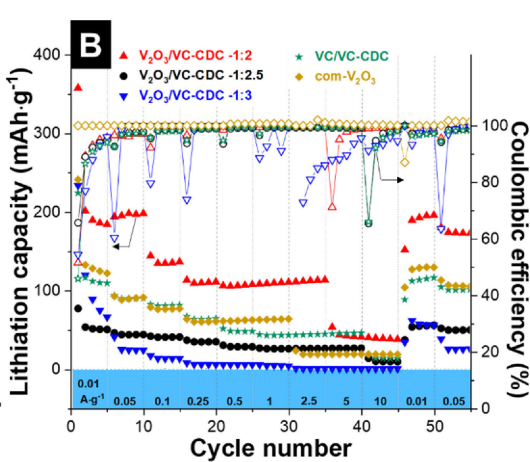


Figure 4. A) The 10th cycle voltage profiles of the samples measured with galvanostatic charge/discharge cycling at a specific current of $0.1 \text{ A} \cdot \text{g}^{-1}$ from 0.01–3.00 V vs. Li/Li⁺. B) Rate handling performance of the samples in the voltage range of 0.01–3.00 V vs. Li/Li⁺.



the second cycle, the highest capacity is obtained for $\text{V}_2\text{O}_3/\text{VC-CDC-1:2}$ ($168 \text{ mAh}\cdot\text{g}^{-1}$), followed by VC-VC-CDC ($111 \text{ mAh}\cdot\text{g}^{-1}$), $\text{com-V}_2\text{O}_3$ ($102 \text{ mAh}\cdot\text{g}^{-1}$), $\text{V}_2\text{O}_3/\text{VC-CDC-1:2.5}$ ($57 \text{ mAh}\cdot\text{g}^{-1}$), and $\text{V}_2\text{O}_3/\text{VC-CDC-1:3}$ ($38 \text{ mAh}\cdot\text{g}^{-1}$). The capacity of $\text{com-V}_2\text{O}_3$ decreased to $27 \text{ mAh}\cdot\text{g}^{-1}$ after 50 cycles, while the capacity of the all other samples increases after the first ten cycles. The capacity increase of VC-VC-CDC electrode proceeded even until the 165th cycle. Afterward, the VC-VC-CDC electrode exhibited a constant capacity of $100 \text{ mAh}\cdot\text{g}^{-1}$. The 500th charge/discharge cycle of $\text{V}_2\text{O}_3/\text{VC-CDC-1:2.5}$ yielded a specific capacity of $90 \text{ mAh}\cdot\text{g}^{-1}$, of $\text{V}_2\text{O}_3/\text{VC-CDC-1:3}$ a value of $40 \text{ mAh}\cdot\text{g}^{-1}$, and of $\text{com-V}_2\text{O}_3$ only $25 \text{ mAh}\cdot\text{g}^{-1}$. The best material $\text{V}_2\text{O}_3/\text{VC-CDC-1:2}$ yielded a capacity of $225 \text{ mAh}\cdot\text{g}^{-1}$ after 500 cycles.

To better understand the cycling performance, we carried out post mortem XRD and Raman analyses (Figure 6A–B) of the electrodes. By this way, we explored possible changes to the structure of V_2O_3 and/or carbon as the possible reason for the improved performance during cycling testing. Considering the metal oxide, we see that the rhombohedral crystal structure of V_2O_3 was maintained in all samples after 500 cycles (Figure 6A). From this finding, we conclude that rhombohedral V_2O_3 is sufficiently stable for lithium intercalation and deintercalation under the conditions we applied for electrochemical cycling. In addition, the XRD results at different lithiation/delithiation states indicate no significant volume changes (Figure S5–6, and Table S3). This contrasts with previous reports that the significant volume change of V_2O_3 during cycling leads to poor capacity retention.^[23,25,47] The comparison of XRD data from the pristine samples and the post mortem analysis of the discharged electrodes after 500 cycles shows no significant residual volume changes of V_2O_3 (Table S1–S2).

As a next step, we investigated possible changes to the structure of carbon in the hybrid materials. Structural changes of carbon can best be studied for the VC-VC-CDC sample. The latter showed an increase of the specific capacity during continuous charge/discharge cycling (Figure 5). While pristine VC-VC-CDC showed a Bragg reflection indicative of hexagonal graphitic carbon at 26.3° 2θ (Figure 1A), this peak has weakened after cycling (Figure 6A). Correspondingly, post mortem Raman analysis (Figure 6B) shows an increased disorder

of carbon per the increased I_D/I_G intensity ratios from 0.9 to 1.2 (Table 1, 4). Similarly, we confirmed an increased I_D/I_G intensity

Table 4. Post mortem Raman spectra analysis of the D and G-modes of the electrodes. FWHM = full-width at half-maximum.

| Sample | Mode | Position [cm ⁻¹] | FWHM [cm ⁻¹] | I_D/I_G |
|--|--------|------------------------------|--------------------------|-----------|
| com- V_2O_3 | D-mode | 1345 | 122 | 0.9 |
| | G-mode | 1589 | 81 | |
| VC-VC-CDC | D-mode | 1353 | 123 | 1.2 |
| | G-mode | 1590 | 67 | |
| $\text{V}_2\text{O}_3/\text{VC-CDC-1:2}$ | D-mode | 1349 | 140 | 2.7 |
| | G-mode | 1599 | 74 | |
| $\text{V}_2\text{O}_3/\text{VC-CDC-1:2.5}$ | D-mode | 1351 | 161 | 2.3 |
| | G-mode | 1599 | 76 | |
| $\text{V}_2\text{O}_3/\text{VC-CDC-1:3}$ | D-mode | 1350 | 99 | 2.2 |
| | G-mode | 1602 | 64 | |

ratio of carbon in $\text{V}_2\text{O}_3/\text{VC-CDC-1:2}$ (from 1.1 to 2.7), $\text{V}_2\text{O}_3/\text{VC-CDC-1:2.5}$ (from 1.1 to 2.3), and $\text{V}_2\text{O}_3/\text{VC-CDC-1:3}$ (from 2.1 to 2.2). The latter shows the smallest change of the carbon phase and the lowest electrochemical performance.

With evident structural changes of the carbon phase and small changes of V_2O_3 , we can now explain the enhanced performance of VC-VC-CDC and all three $\text{V}_2\text{O}_3/\text{VC-CDC}$ samples: Seemingly, the ability of carbon in the hybrid material electrodes to reversibly store and release lithium is improved over the course of continued charge/discharge cycling. This ability benefits the overall performance because the low minimum voltage limit of 0.01 V vs. Li/Li^+ allows lithium intercalation into (graphitic) carbon.

3. Conclusions

We present a simplified synthesis for V_2O_3 /carbon hybrid materials. In the first step, $\text{NiCl}_2\cdot 6\text{H}_2\text{O}$ reacts with vanadium carbide to concurrently produce rhombohedral V_2O_3 and carbon. During the decomposition of $\text{NiCl}_2\cdot 6\text{H}_2\text{O}$, vanadium is selectively etched, leaving behind nanoporous carbide-derived carbon with a disordered structure. Locally, the residual nickel

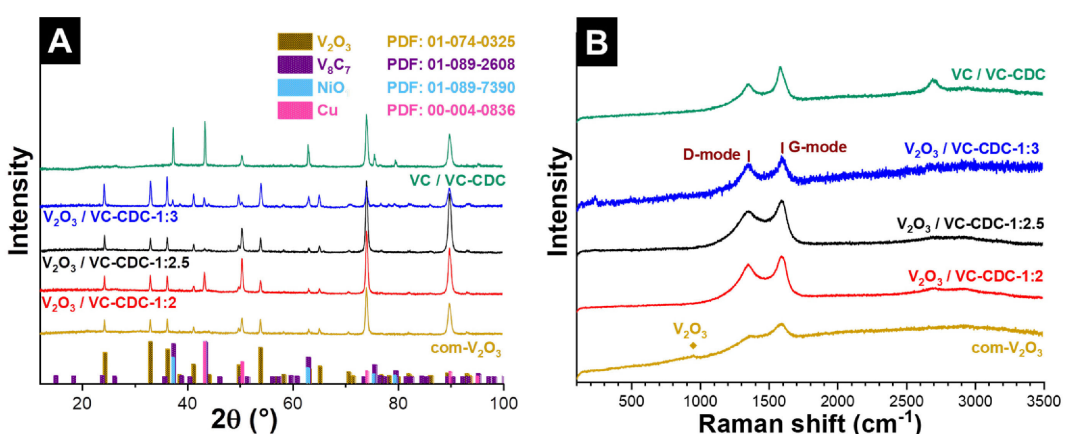


Figure 6. A) XRD pattern and B) Raman spectra of the samples after 500 cycles.

leads to the formation of carbon with a much higher degree of graphitic ordering. After the one-step thermal annealing, the remaining metallic nickel can easily be removed from the sample by washing in aqueous HCl. We tested the electrochemical performance in the broad voltage window of 0.01–3.0 V vs. Li/Li⁺. The best electrochemical performance of V₂O₃/VC-CDC hybrid material as an anode for LIBs with a half-cell configuration was 187 mAh·g⁻¹ at a low rate of 0.01 A·g⁻¹ and still 105 mAh·g⁻¹ at the high specific current of 2.5 A·g⁻¹. This performance was much better compared to commercially available V₂O₃ mixed with the same amount of carbon as present in our hybrid system; the composite electrode only had an initial specific capacity of 18 mAh·g⁻¹ at the specific current of 2.5 A·g⁻¹. With the very low potential of 0.01 V vs. Li/Li⁺, the adaptation of the materials presented in our study may also carefully consider the possible issue of electroplating.

Supporting Information

Thermogravimetric data with coupled mass spectra, scanning electron micrographs, nitrogen gas sorption isotherms, Raman peak fitting analysis, scanning transmission electron micrographs, and results from the Rietveld analysis.

Acknowledgments

The authors thank Eduard Arzt (INM) for his continuing support. The INM team acknowledges the funding of the COSH-CDC project (PR-1173/5-1) by the German Research Foundation (DFG). This work was part of the Carbon Metal Oxide Nanohybrid project (CarMON) supported by the Leibniz Association (SAW-2017). The authors thank Mesut Aslan, Jaehoon Choi, Robert Drumm, Ingrid Grobelsek, Benjamin Krüner, Eunho Lim, and Rafael Linzmeyer Zornitta (all at INM) for technical support and helpful discussions.

Conflict of Interest

The authors declare no conflict of interest.

Keywords: anode materials • carbide-derived carbon • hybrid materials • lithium-ion batteries • vanadia

- [1] N. Nitta, F. Wu, J. T. Lee, G. Yushin *Mater. Today*. **2015**, *18*, 252–264.
- [2] Z. Yang, J. Zhang, M. C. Kintner-Meyer, X. Lu, D. Choi, J. P. Lemmon, J. Liu *Chem. Rev.* **2011**, *111*, 3577–3613.
- [3] M. Armand, J. M. Tarascon *Nature*. **2008**, *451*, 652.
- [4] M. Broussely, G. Archdale *J. Power Sources*. **2004**, *136*, 386–394.
- [5] P. Geng, S. Zheng, H. Tang, R. Zhu, L. Zhang, S. Cao, H. Xue, H. Pang *Adv. Energy Mater.* **2018**, *8*, 1703259.
- [6] J. M. Tarascon, M. Armand *Nature*. **2001**, *414*, 359.
- [7] Z. Zhang, S. S. Zhang, Rechargeable Batteries, Springer International Publishing Cham, 2015.
- [8] N. A. Kaskhedikar, J. Maier *Adv. Mater.* **2009**, *21*, 2664–2680.
- [9] G. N. Zhu, Y. G. Wang, Y. Y. Xia *Energy Environ. Sci.* **2012**, *5*, 6652–6667.

- [10] F. Joho, B. Rykart, R. Imhof, P. Novak, M. E. Spahr, A. Monnier *J. Power Sources*. **1999**, *81*–82, 243–247.
- [11] S. Goriparti, E. Miele, F. De Angelis, E. Di Fabrizio, R. P. Zaccaria, C. Capiglia *J. Power Sources*. **2014**, *257*, 421–443.
- [12] J. R. Dahn, T. Zheng, Y. Liu, J. S. Xue *Science*. **1995**, *270*, 590–593.
- [13] T. Song, J. Xia, J. H. Lee, D. H. Lee, M. S. Kwon, J. M. Choi, J. Wu, S. K. Doo, H. Chang, W. I. Park, D. S. Zang, H. Kim, Y. Huang, K. C. Hwang, J. A. Rogers, U. Paik *Nano Lett.* **2010**, *10*, 1710–1716.
- [14] M. Widmaier, K. Pfeifer, L. Bommer, V. Presser *Batteries & Supercaps*. **2018**, *1*, 11–26.
- [15] E. Lim, H. Shim, S. Fleischmann, V. Presser *J. Mater. Chem. A*. **2018**, *6*, 9480–9488.
- [16] C. Z. Wu, Y. Xie *Energy Environ. Sci.* **2010**, *3*, 1191–1206.
- [17] G. Silversmit, D. Depla, H. Poelman, G. B. Marin, R. De Gryse *J. Electron Spectrosc. Relat. Phenom.* **2004**, *135*, 167–175.
- [18] S. Fleischmann, A. Tolosa, V. Presser *Chem. Eur. J.* **2018**, *24*, 12143–12153.
- [19] N. A. Chernova, M. Roppolo, A. C. Dillon, M. S. Whittingham *J. Mater. Chem.* **2009**, *19*, 2526–2552.
- [20] M. Zeiger, T. Ariyanto, B. Krüner, N. J. Peter, S. Fleischmann, B. J. M. Etzold, V. Presser *J. Mater. Chem. A*. **2016**, *4*, 18899–18909.
- [21] T. Kudo, Y. Ikeda, T. Watanabe, M. Hibino, M. Miyayama, H. Abe, K. Kajita *Solid State Ionics*. **2002**, *152*–153, 833–841.
- [22] T. E. Ashton, D. Hevia Borras, A. Iadecola, K. M. Wiaderek, P. J. Chupas, K. W. Chapman, S. A. Corr *Acta Crystallogr. Sect. B* **2015**, *71*, 722–726.
- [23] L. Jiang, Y. Qu, Z. Ren, P. Yu, D. Zhao, W. Zhou, L. Wang, H. Fu *ACS Appl. Mater. Interfaces*. **2015**, *7*, 1595–1601.
- [24] Y. Shi, Z. J. Zhang, D. Wexler, S. L. Chou, J. Gao, H. D. Abruna, H. J. Li, H. K. Liu, Y. P. Wu, J. Z. Wang *J. Power Sources*. **2015**, *275*, 392–398.
- [25] Y. F. Sun, S. S. Jiang, W. T. Bi, C. Z. Wu, Y. Xie *J. Power Sources*. **2011**, *196*, 8644–8650.
- [26] Y. Yan, B. Li, W. Guo, H. Pang, H. Xue *J. Power Sources*. **2016**, *329*, 148–169.
- [27] D. McNulty, D. N. Buckley, C. O'Dwyer *ChemElectroChem*. **2017**, *4*, 2037–2044.
- [28] M. R. Lukatskaya, B. Dunn, Y. Gogotsi *Nat. Commun.* **2016**, *7*, 12647.
- [29] M. Widmaier, N. Jäckel, M. Zeiger, M. Abuzarli, C. Engel, L. Bommer, V. Presser *Electrochim. Acta*. **2017**, *247*, 1006–1018.
- [30] A. Odani, V. G. Pol, S. V. Pol, M. Koltypin, A. Gedanken, D. Aurbach, *Adv. Mater.* **2006**, *18*, 1431–1436.
- [31] L. Zeng, C. Zheng, J. Xi, H. Fei, M. Wei *Carbon*. **2013**, *62*, 382–388.
- [32] S. Brunauer, P. H. Emmett, E. Teller *J. Am. Chem. Soc.* **1938**, *60*, 309–319.
- [33] G. Y. Gor, M. Thommes, K. A. Cychoz, A. V. Neimark *Carbon*. **2012**, *50*, 1583–1590.
- [34] V. Presser, M. Heon, Y. Gogotsi *Adv. Funct. Mater.* **2011**, *21*, 810–833.
- [35] T. Ariyanto, A. M. Kern, B. J. M. Etzold, G. R. Zhang *Electrochim. Commun.* **2017**, *82*, 12–15.
- [36] A. C. Ferrari, D. M. Basko *Nat. Nanotechnol.* **2013**, *8*, 235.
- [37] A. C. Ferrari *Solid State Commun.* **2007**, *143*, 47–57.
- [38] H. J. T. Ellingham *J. Soc. Chem. Ind.* **1944**, *63*, 125–133.
- [39] R. Dash, J. Chmiola, G. Yushin, Y. Gogotsi, G. Laudisio, J. Singer, J. Fischer, S. Kucheyev *Carbon*. **2006**, *44*, 2489–2497.
- [40] C. R. Perez, S.-H. Yeon, J. Segalini, V. Presser, P.-L. Taberna, P. Simon, Y. Gogotsi *Adv. Funct. Mater.* **2013**, *23*, 1081–1089.
- [41] M. Zeiger, N. Jäckel, V. N. Mochalin, V. Presser *J. Mater. Chem. A*. **2016**, *4*, 3172–3196.
- [42] R. Fu, T. F. Baumann, S. Cronin, G. Dresselhaus, M. S. Dresselhaus, J. H. Satcher, Jr. *Langmuir*. **2005**, *21*, 2647–2651.
- [43] M. Thommes, K. Kaneko, A. V. Neimark, J. P. Olivier, F. Rodriguez-Reinoso, J. Rouquerol, K. S. W. Sing *Pure Appl. Chem.* **2015**, *87*, 1051–1069.
- [44] A. P. Cohn, L. Oakes, R. Carter, S. Chatterjee, A. S. Westover, K. Share, C. L. Pint *Nanoscale*. **2014**, *6*, 4669–4675.
- [45] S. J. An, J. L. Li, C. Daniel, D. Mohanty, S. Nagpure, D. L. Wood *Carbon*. **2016**, *105*, 52–76.
- [46] A. Iturrondebeitia, A. Goni, I. Gil de Muro, L. Lezama, T. Rojo *Nano-materials*. **2017**, *7*, 423.
- [47] B. Xiao, B. Zhang, L. B. Tang, C. S. An, Z. J. He, H. Tong, W. J. Yu, J. C. Zheng *Ceram. Int.* **2018**, *44*, 15044–15049.

Manuscript received: October 27, 2018
Version of record online: December 7, 2018